Insight into winter haze formation mechanisms based on aerosol hygroscopicity and effective density measurements

Yuanyuan Xie[1], Xingnan Ye[1,2]*, Zhen Ma[1], Ye Tao[1], Ruyu Wang[1], Ci Zhang[1], Xin Yang[1,2], Jianmin Chen[1,2], Hong Chen[1]

[1]Shanghai Key Laboratory of Atmospheric Particle Pollution and Prevention (LAP3), Department of Environmental Science and Engineering, Fudan University, Shanghai 200433, China.

[2] Institute of Atmospheric Sciences, Fudan University, Shanghai 200433, China.

*Correspondence to: Xingnan Ye (yexingnan@fudan.edu.cn) and Jianmin Chen (jmchen@fudan.edu.cn).

Abstract: We characterize a representative particulate matter (PM) episode that occurred in Shanghai during winter 2014. Particle size distribution, hygroscopicity, effective density, and single particle mass spectrometry were determined online, along with offline analysis of water-soluble inorganic ions. The mass ratio of SNA/$PM_{1.0}$ (sulfate, nitrate, and ammonium) fluctuated slightly around 0.28, suggesting that both secondary inorganic compounds and carbonaceous aerosols contributed substantially to the haze formation, regardless of pollution level. Nitrate was the most abundant ionic species during hazy periods, indicating that NO_x contributed more to haze formation in Shanghai than did SO_2. During the representative PM episode, the calculated PM was always consistent with the measured $PM_{1.0}$, indicating

18 that the enhanced pollution level was attributable to the elevated number of larger particles. The number

19 fraction of the near-hydrophobic group increased as the PM episode developed, indicating the

20 accumulation of local emissions. Three "banana-shaped" particle evolutions were consistent with the

21 rapid increase of $PM_{1.0}$ mass loading, indicating that the rapid size growth by the condensation of

22 condensable materials was responsible for the severe haze formation. Both hygroscopicity and effective

23 density of the particles increased considerably with growing particle size during the banana-shaped

24 evolutions, indicating that the secondary transformation of NO_x and SO_2 was one of the most important

25 contributors to the particle growth. Our results suggest that the accumulation of gas-phase and particulate

26 pollutants under stagnant meteorological conditions and subsequent rapid particle growth by secondary

27 processes, were primarily responsible for the haze pollution in Shanghai during wintertime.

28 **Keywords**: air pollution; size distribution; hygroscopic growth; secondary process; Shanghai.

30 **1. Introduction**

31 Atmospheric aerosol has significant influences on radiation balance and climate forcing of the

32 atmosphere (Wang et al., 2011;Wang et al., 2014c;Wu et al., 2016a;IPCC, 2013). Also, atmospheric

33 aerosol has strong impacts on visibility (Yang et al., 2012;Lin et al., 2014;Xiao et al., 2014) and public

34 health (Heal et al., 2012). Recent studies found that short-term exposure to haze pollution could cause

35 airway inflammation and aggravate respiratory symptoms in chronic obstructive pulmonary disease

36 patients (Wu et al., 2016b;Guan et al., 2016).

37 With the huge achievements in economic development and rapid urbanization over the past 30 years,

38 particulate pollution has become a major environmental concern in China. The most severe haze event

39 that occurred in the first quarter of 2013, spread over 1.6 million km^2 (Wang et al., 2014a). This event

40 motivated the release of the Action Plan on Prevention and Control of Air Pollution with the goal of

41 reducing $PM_{2.5}$ (particulate matter smaller than 2.5 μm in aerodynamic diameter) concentration by 15−25%

42 in   2017   against   2012   in   three   major   city   clusters

43 (http://english.mep.gov.cn/News_service/infocus/201309/t20130924_260707.htm). In order to reduce

44 the $PM_{2.5}$ concentration, extensive studies have been conducted to investigate the sources and formation

45 mechanisms of haze pollution in recent years (Ye et al., 2011;Sun et al., 2016;Qiao et al., 2016;Hu et al.,

46 2016;Li et al., 2016;Guo et al., 2014;Zheng et al., 2015;Guo et al., 2013;Wang et al., 2016;Peng et al.,

47 2016). However, the haze formation mechanisms and source appointment of fine particles remain

48 uncertain.

49 Guo et al. (2013) summarized historical reports from 2000 to 2008 in Beijing and found that the

50 origins of urban fine particles varied in different seasons: the contribution of primary emissions is

51 comparable to that of secondary formation during winter heating periods whereas secondarily produced

52 aerosols dominate the fine PM sources in other seasons. As an important type of primary emissions in

53 urban area, black carbon (BC) is primarily from incomplete fossil fuel combustion. Light absorption of

54 BC aerosols is increased after atmospheric aging by coating with secondary materials and restructuring

55 (Khalizov et al., 2009). Due to cooling effect at the surface and warming effect aloft, the enhanced light

56 absorption and scattering by aged BC particles stabilize the atmosphere, hindering vertical transport of

57 gaseous and particulate pollutants (Wang et al., 2013). BC aging occurs much more efficiently in the

58 presence of highly elevated gaseous aerosol precursors so that light absorption increases by a factor of

59 2.4 within 4.6 h under highly polluted conditions in Beijing, significantly exacerbating pollution

60 accumulation and strongly contributing to severe haze formation (Peng et al., 2016).

61   Due to the implement of several effective regulatory policies, the increasing trend of primary

62 emissions has been under control since the 11th five-year period. A growing number of studies suggested

63 that secondary production was the major contributor to the haze events in recent years (Shi et al.,

64 2014;Zhao et al., 2013;Zhang et al., 2015a;Huang et al., 2014), in contrast with the fact that primary

65 emissions were of great importance in some haze events (Niu et al., 2016). Guo et al. (2014) reported that

66 the development of PM episodes in Beijing was characterized by efficient nucleation and continuous

67 particle growth over an extend period dominated by local secondary formation. They attributed the

68 continuous growth of particle size and constant accumulation of particle mass concentration to the highly

69 elevated concentrations of gaseous precursors such as NO_x, SO_2, and volatile organic compounds (VOCs),

70 while the contribution from primary emissions and regional transport was negligible. However, the role

71 of regional transport of $PM_{2.5}$ in haze formation remains controversial (Li et al., 2015;Zhang et al., 2015b).

72   The most important advances in the understanding of urban PM formation were reviewed by Zhang

73   et al. (2015c). The concentrations of SO_2, NO_x, and anthropogenic source VOCs in Beijing and other

74   cities of the developing world are significantly higher than those in the urban areas of developed countries,

75   resulting in large secondary production of sulfate, nitrate, and SOA. Synergetic effects among various

76   organic and inorganic compounds may exist under highly polluted conditions, indicating different PM

77   formation rates between developing and developed urban regions. Indeed, a large enhancement of

78   particulate sulfate was typically observed during regional haze events in China (Chen et al., 2016;Wang

79   et al., 2015;Fu et al., 2008;Xie et al., 2015). Currently, the highly elevated sulfate concentration during

80   haze events cannot be fully explained by model simulations (Wang et al., 2014b;Chen et al., 2016).

81   Recently, a significant breakthrough made by Wang et al. (2016) has provided a reasonable explanation

82   about the high level of sulfate during haze events. It was revealed by their laboratory experiments that the

83   aqueous oxidation of SO_2 by NO_2 proceeds more efficiently with the increase of NO_2 concentration

84   whereas the reaction is suppressed in acid conditions, because acid effect reduces the solubility of SO_2

85   and reaction rate. The enhanced sulfate formation during severe haze periods in Beijing was attributable

86   to aqueous oxidation of SO_2 by NO_2 on hygroscopic fine particles under conditions of elevated RH and

87   the concentrations of NH_3 and NO_2, as confirmed by the comparable SO_2 uptake coefficients for sulfate

88   formation from field and laboratory results.

89   The hygroscopic properties of ambient particles vary significantly depending on the origin of the air

90   masses and the atmospheric aging process. In urban air, the population of near-hydrophobic particles can

91   be assumed to consist largely of freshly emitted combustion particles containing high mass fractions of

92   soot and water-insoluble organic compounds (Swietlicki et al., 2008;Massling et al., 2009). In contrast,

93   secondary sulfate or nitrate aged particles are more-hygroscopic, and their relative abundance is primarily

94   responsible for the hygroscopic growth of ambient particles at elevated RH (Topping et al.,

95   2005;Aggarwal et al., 2007;Gysel et al., 2007). Thus, hygroscopicity can serve as a tracer of source origins,

96   mixing state, and aging mechanisms of ambient particles. For example, the temporal variation of aerosol

97   hygroscopicity has thrown some new light on haze formation mechanisms in Beijing and Shanghai (Ye

98   et al., 2011;Guo et al., 2014).

99   Density is one of the most important physicochemical properties for atmospheric aerosols. Effective

100   density has served as a tracer for new particle formation and for the aging process in previous studies (Yin

101   et al., 2015;Guo et al., 2014). The ambient particles in urban areas are mostly complex mixtures of

102   elemental carbon (EC), organics (OC), and secondary inorganic aerosols (SIA) (Hu et al., 2012). The

103   effective density of nascent traffic particles varies from approximately 0.9 g cm^{-3} to below 0.4 g cm^{-3},

104   decreasing with the increase of particle size, because there are more voids between primary particles in

105   relatively larger aggregates (Momenimovahed and Olfert, 2015). The effective density of OC is in

106   between those of EC and SIA, and varies with source. The effective density of combustion particles

107   increases by filling the voids in the agglomerate particles with condensed semi-volatile materials, or by

108   restructuring agglomerates with hygroscopic SIA (Momenimovahed and Olfert, 2015;Zhang et al., 2008).

109   In this study, a combined HTDMA-APM system was used to investigate the variations of

110   hygroscopicity and effective density of submicrometer aerosols during winter 2014 in urban Shanghai. In

111   addition, cascade impactor samples were collected and temporal variations of particle composition were

112   determined by a single particle mass spectrometry, which provided further insight into the hygroscopicity

113   and density variations. The primary objectives of this study were to investigate the particle growth

114   mechanisms and to identify the contribution of local emissions during the winter haze events.

115

116   **2. Experimental**

117   **2.1. Sampling site**

118   The measurements of particle hygroscopicity and effective density were conducted from 21 December

119   2014 to 13 January 2015 at the Department of Environmental Science and Engineering in the main

120   campus of Fudan University (31.30° N, 121.5° E). It can be considered as a representative urban site for

121   Shanghai. There are many dwelling quarters and commercial blocks in surrounding area. About 400 m

122   away from the measurement site, there is the Middle Ring Line, one of the busiest elevated roads in the

123   city.

124   **2.2 Measurements of air quality index and ground meteorological parameters**

125   At a supersite about 100 m away from the Environmental Building, $PM_{1.0}$ was monitored using a

126   Thermo Scientific™ 5030 SHARP monitor. Trace gas pollutants were monitored using Thermo

127   Scientific™ i-series gas analyzers (43i for SO_2, 49i for O_3, 42i for $NO/NO_2/NO_x$), and meteorological

128   data were monitored using an automatic meteorological station (Model CAWS600, Huayun Inc., China)

129   (Yin et al., 2015). The datas of $PM_{2.5}$, PM_{10}, and CO were released by the Shanghai Environmental

130   Monitoring Center. The height of the Planet Boundary Layer (PBL) was computed online using the NCEP

131   Global Data Assimilation System (GDAS) model (http://ready.arl.noaa.gov/READYamet.php).

132   **2.3. HTDMA-APM system**

133   Particle size distribution, hygroscopic growth factor (GF), and effective density were measured using

134   a custom-built HTDMA-APM system (Fig. 1). The custom-built HTDMA (Hygroscopic Tandem

135   Differential Mobility Analyzers) mainly consist of two long DMAs (3081L, TSI Inc.), a humidifier (PD-

136   50T-12MSS, Perma Pure Inc.) and a Condensation Particle Counter (CPC, Model 3771, TSI Inc.). A

137   detailed description of the HTDMA is available in Ye et al. (2009). In this observation, particle number

138   size distribution in the range of 14−600 nm and hygroscopic growth at 83% RH for particles with dry

139   diameters of 40, 100, 220, 300, 350, and 400 nm were determined by HTDMA in turn. The determination

140   of effective density by DMA-APM was described previously (Yin et al., 2015;Pagels et al., 2009). Briefly,

141   a combined system consisting of a compact Aerosol Particle Mass Analyzer (APM, Model 3601,

142   Kanomax Inc.) and a CPC (Model 3775, TSI Inc.) was connected to the sample tubing through a 3-way

143   electrical switch behind the upstream DMA (DMA1). The APM comprises two coaxial cylindrical

144 electrodes rotating at the same angular velocity. Charged aerosol particles of a certain diameter sized by

145 DMA1 are axially fed into the annular gap between the electrodes and experienced an outward centrifugal

146 force from the particle rotating and an inward electrostatic force from the high-voltage field between the

147 electrodes. Particles pass through the APM and are sent to the CPC when the two forces are balanced.

148 The mass of particles that pass through the APM is determined by the rotation rate and the applied voltage.

149 Effective densities for dry diameters of 40, 100, 220, and 300 nm were determined by the method of

150 DMA-APM in this study. The HTDMA-APM was operated alternatively in HTDMA mode and then

151 DMA-APM mode, for every 40 min.

152   Before the field observation, the HTDMA-APM was calibrated using 40–450 nm NIST-Traceable PSL

153 particles and ammonium sulfate. The measured HTDMA data were inversed with the $TDMA_{inv}$ algorithm

154 to obtain the actual GF distribution. This is because the raw data are only a skewed and smoothed integral

155 transform of the actual growth factor probability density function (GF-PDF) (Gysel et al., 2009). The

156 hygroscopicity parameter κ was derived from the GF data after inversion with the $TDMA_{inv}$ algorithm

157 according to the κ-Köhler theory (Petters and Kreidenweis, 2007).

158 **2.4. SPAMS**

159   A Single Particle Aerosol Mass Spectrometry (SPAMS, Hexin Analytical Instrument Co., Ltd., China)

160 installed in the same room with the HTDMA-APM system was used to obtain the chemical and size

161 information of individual particles in the range of 0.2–2 μm. Detailed information on SPAMS is available

162   in Li et al. (2011). Briefly, ambient particles are drawn into a vacuum chamber through an aerodynamic

163   focusing lens and accelerated to a size-dependent terminal velocity. Sized particles are desorbed and

164   ionized by the pulsed desorption/ionization laser (Q-switched Nd: YAG, λ=266 nm) at the ion source

165   region. Both positive and negative mass spectra for a single particle are recorded by a bipolar time-of-

166   flight spectrometer. The single particle information was imported into YAADA (version 2.11,

167   www.yaada.org). Based on the similarities of the mass-to-charge ratio and peak intensity, particles were

168   classified using the ART-2a method.

169   **2.5. Ion chromatography**

170   Cascade impactor aerosol samples for offline analysis were collected at the roof platform of the

171   Environmental Building using a 10-stage MOUDI sampler (Micro-Orifice Uniform Deposit Impactor,

172   Model 110-NR, MSP Corp., USA). Detailed description of the sampling, pretreatment, chemical analysis,

173   and quality control of this system is available in Tao et al. (2016). Briefly, cascade impactor samples were

174   collected every 24 h using the PALL7204 quartz filter as the collection substrate. Each filter was weighted

175   with a BP211D electronic balance at $25\pm1°C$ and $40\pm2\%RH$. The water extract of each sample was

176   analyzed using an Ion Chromatograph (Metrohm 883 basic IC plus, Switzerland) equipped with a third-

177   party column heater (CT-100, Agela Corp., China). Seven anions (F^-, Cl^-, NO_2^-, Br^-, NO_3^-, SO_4^{2-} and PO_4^{3-})

178   were resolved using a Metrosep A Supp 5-250/4.0 column at 35°C with an eluent of 3.2 mmol L^{-1} Na_2CO_3

179   + 1.0 mmol L^{-1} $NaHCO_3$. Six cations (Li^+, Na^+, NH_4^+, K^+, Ca^{2+}, and Mg^{2+}) were separated by a Metrosep

180 C4-250/4.0 column at 30°C with an eluent of 1.7 mmol L^{-1} HNO_3 + 0.7 mmol L^{-1} 2,6-pyridine

181 dicarboxylic acid.

182

183 **3. Results and discussion**

184 **3.1. Periodic cycle of PM episodes during the observation period**

185 Figure 2 shows the temporal variations of PM mass loading during the winter observation (21

186 December 2014 to 13 January 2015). The official data of $PM_{2.5}$ and PM_{10} were blank on some clean days.

187 Meteorologically, our measurement was deployed in a typical winter period. The average concentrations

188 of $PM_{1.0}$, $PM_{2.5}$, and PM_{10} were 57 ± 37, 87 ± 67, and 129 ±78 μg m^{-3}, respectively. About 62% of hourly

189 averaged $PM_{2.5}$ concentrations exceeded 75 μg m^{-3} of the Chinese Grade II guideline (GB 3095-2012),

190 indicating heavy particle pollution in Shanghai during wintertime. The PM episodes exhibited a clear

191 periodic cycle of ~5 days. A similar feature was previously observed in Beijing (Guo et al., 2014). At the

192 beginning of each cycle, the $PM_{1.0}$ level was below 35 μg m^{-3}. Generally, the difference between the

193 concentrations of $PM_{1.0}$ and $PM_{2.5}$ during clean days was less significant than that in haze periods.

194 Occasionally the measured $PM_{2.5}$ concentrations were larger than those of PM_{10}, possibly due to system

195 error. However, the particle mass concentration began to increase in the next few days, with $PM_{1.0}$ and

196 $PM_{2.5}$ peaking at over 100 and 200 μg m^{-3}, respectively. During the end of each PM episode, the change

197 in weather conditions played a key role in the decrease of particle concentration. As shown in Fig. S1, the

198   prevailing winds on haze days were from the northwest. The prevailing winds during two clean periods

199   (25–27 December and 12–14 January) were northeasterly, bringing clean air mass from East China Sea.

200   Two cold fronts from the north swept Shanghai on 31 December and 6 January, bringing gale and lower

201   temperature which favored the dispersion of atmospheric pollutants.

202   **3.2 Contributions of secondary inorganic aerosols to $PM_{1.0}$ mass loading**

203   Figure 3 illustrates the daily concentrations of sulfate, nitrate, and ammonium as a function of $PM_{1.0}$

204   mass loading. In general, the sum of concentrations of sulfate, nitrate, and ammonium (SNA) increased

205   linearly as the $PM_{1.0}$ mass loading increased. It is noticeable that the $SNA/PM_{1.0}$ ratio slightly fluctuated

206   around 0.28, regardless of the pollution level. Because soil dust and sea salt made a negligible contribution

207   to the fine particle mass concentration in this study, the almost constant ratio of $SNA/PM_{1.0}$ indicates that

208   SNA and carbonaceous aerosols (including soot and organic matter) synchronously increased during the

209   haze events. As the $PM_{1.0}$ concentration increased, the concentration of nitrate increased more rapidly

210   than sulfate so that it became the most abundant ionic species at $PM_{1.0} > 40$ μg m^{-3}. This finding indicates

211   that NO_x contributed more to haze formation in Shanghai compared to SO_2. Generally, the visibility

212   decreased with the increase in PM concentration, indicating photochemical activity began to weaken as

213   the development of haze events. The large increase in nitrate concentration may be attributable to

214   heterogeneous reaction on the preexisting particles. Nitrate formation is highly dependent on the surface

215   area of preexisting particles and is favored under NH_3-rich conditions (Chu et al., 2016). In contrast, Han

216 et al. (2016) reported that the mass ratio of nitrate to sulfate decreased with the increase of $PM_{2.5}$ level

217 and that the sources of sulfate contributed more to the haze formation in Beijing than mobile sources.

218 This finding suggests that the haze formation mechanism in Shanghai is likely different from that in

219 Beijing. VOCs and NO_x are exclusively from local emissions whereas regional transport is a big source

220 of SO_2 under stagnant atmosphere, due to different atmospheric lifetimes among SO_2, NO_x, and VOCs

221 (Guo et al., 2014). Considering the relatively smaller contribution of sulfate, our results reveal that the

222 accumulation and secondary transformation of local emissions likely played a dominant role in this haze

223 formation.

224 **3.3 Aerosol hygroscopicity and effective density during the observation period**

225 Figure 4a displays a box chart of the mean hygroscopicity of each hygroscopic growth factor

226 distribution for different sizes. Considering all of the growth factor distributions collectively, the

227 hygroscopicity parameter κ increased with increase of the dry diameter, with a mean κ of 0.161 at 40 nm

228 and 0.338 at 300 nm. Assuming a two-component system of a model salt (ammonium sulfate, $\kappa_m = 0.53$)

229 and an insoluble species ($\kappa = 0$), the volume fraction of hygroscopic species (ε) can be obtained based on

230 the Zdanovskii−Stokes−Robinson (ZSR) mixing rule. The average ε was 0.3 for 40 nm particles,

231 suggesting that the primary particles or initial growth of freshly generated particles were dominated by

232 non-hygroscopic species. In contrast, the 300 nm particles were extremely aged, with more-hygroscopic

233 species.

234   Generally, HTDMAs measure dry particles smaller than 300 nm due to technical limitations, and it is

235   common that particle hygroscopicity increases with the increase of particle size (Liu et al.,

236   2014;Swietlicki et al., 2008). The increase of particle hygroscopicity with particle size was attributed to

237   the addition of more-hygroscopic SNA (Swietlicki et al., 2008;Ye et al., 2010). The very few

238   measurements for dry particles larger than 300 nm showed different size dependencies. Gasparini et al.

239   (2006) reported that particle hygroscopicity first increased and then decreased with the increase of particle

240   size, peaking at the diameter of 300 nm. In contrast, Wu et al. (2016c) reported that particle hygroscopicity

241   increased with particle diameter in the range of 35-350 nm. In this study, the determination size range

242   was extended to 400 nm and the mean κs of 300, 350, and 400 nm particles were nearly equal. We attribute

243   the different size dependencies of hygroscopicity among various measurement sites to the total emissions

244   of SO_2 and NO_x, gas precursors of hygroscopic sulfate and nitrate. It is noticeable that the 5th percentile

245   hygroscopicity decreased for dry diameter larger than 300 nm, likely due to the presence of the smallest

246   dust particles (Gasparini et al., 2006). The variability of hygroscopicity parameter κ was much greater for

247   40 nm particles. The particle population with $\kappa < 0.1$ was attributed to fresh traffic particles (Ye et al.,

248   2013). The considerable percentile of $\kappa < 0.1$ indicates that the 40 nm particle population was sometimes

249   dominated by near-hydrophobic particles.

250   Figure 4b displays a box chart of median effective density for different particle sizes. The median

251   effective density varied in the narrow range of $\rho_{eff} = 1.35-1.41$ g cm^{-3} for 40–300 nm particle population.

252   The size dependency of particle effective density varied in the literature. Hu et al. (2012) and Yin et al.

253   (2015) reported that effective density of the particles increased as particle size increased while a opposite

254   trend was observed by Geller et al. (2006) and Spencer et al. (2007). The different trends were attributable

255   to the variable fraction of lower density mode particles ($\rho_{eff} < 1.0$ g cm^{-3}). The densities of the secondarily

256   produced $(NH_4)_2SO_4$, NH_4HSO_4, and NH_4NO_3 are ~1.75 g cm^{-3}. The effective density of organic aerosols

257   varies mostly in the range of 1.2-1.6 g cm^{-3}, depending on their source origins (Malloy et al., 2009;Turpin

258   and Lim, 2001;Dinar et al., 2006). The lower density particles with $\rho_{eff} < 1.0$ g cm^{-3} were attributable to

259   fresh or partially aged traffic-related particles, because the number fraction of the lower density group in

260   urban area was found to be consistent with the concentration of NO (indicator of traffic) (Levy et al.,

261   2013;Rissler et al., 2014). Although the dominant accumulation mode particles have an effective density

262   greater than Aitken mode ones, the presence of a lower effective density group associated with traffic

263   emissions might decrease the mean effective density to a value lower than that of Aitken mode particles

264   (Levy et al., 2014). Yin et al. (2015) reported that effective density distributions were dominated by a

265   single peak in the previous observation. In contrast, a lower density peak below 1.0 g cm^{-3} was often

266   present in this observation, decreasing the mean effective density of externally mixed aerosols.

267   **3.4 Characteristics of a representative PM episode**

268   As shown in Fig. 2, the PM episode from 7 to 12 January was a representative case of severe haze

269   formation and elimination processes. It can be divided into clean (7 January), transition (8 January), haze

270   (9−11 January), and post-haze (12 January) periods. During the transition from the clean period to haze

271   period (7 to 8 January), both $PM_{1.0}$ and $PM_{2.5}$ concentrations increased slightly, with an average

272    $PM_{1.0}/PM_{2.5}$ ratio of 0.65. A sharp increase in $PM_{2.5}$ (of 125 µg m^{-3}) was observed from 6:00 to 12:00 LT

273   on the morning of 9 January. During the haze period, the concentration of $PM_{2.5}$ exceeded 115 µg m^{-3}

274   (medially polluted level, HJ633-2012) for 63 h. On 11 January, the hourly $PM_{2.5}$ concentration exceeded

275   250 µg m^{-3}, corresponding to the severely polluted level.

276   Figure 5 displays the temporal profile of particle size distribution, along with the measured $PM_{1.0}$

277   concentration during the representative PM episode. The calculated PM concentrations (PM_{cal}) were

278   obtained based on the particle size distribution and average effective density of 1.39 g m^{-3} in the range of

279   14−600 nm measured in this study. It is noticeable that the temporal trends in mass concentrations of

280   PM_{cal} and $PM_{1.0}$ are highly consistent. In contrast to the fact that particle size distribution was dominated

281   by nanoparticles during the clean period, the burst of Aitken mode particles and subsequent continuous

282   growth to approximately 200 nm in diameter was observed three times during the haze period, indicating

283   that the presence of numerous larger particles is likely responsible for the severe particle pollution (Guo

284   et al., 2014). The importance of larger particles in haze formation is also illustrated by the contour plot of

285   the particle volume size distribution. The difference of particle number concentration between transition

286   and haze periods was less significant, whereas the volume concentration increased considerably during

287   the haze period. This feature clearly demonstrates that the haze formation was closely correlated with

288   particle growth and elevated number of larger particles.

289   Interestingly, the particle mass concentration was sensitive to variations of wind speed and planetary

290   boundary layer (PBL). During the transition and haze periods, the wind speed decreased considerably

291   with insignificant change in prevailing wind (Fig. S1). This finding indicates that outside transportation

292   became less and less significant. It is noteworthy that the temporal evolution of the particle mass

293   concentration was inversely correlated with the PBL height. The decreasing PBL provided a stagnant

294   atmosphere that favored the accumulation of local emissions. This finding reveals that the severe haze

295   pollution was likely triggered by the adverse meteorological conditions. The impact of decreasing PBL

296   height on haze formation can also be evidenced by the variations of trace gaseous species (Fig. S2).

297   During the PM episode, the concentrations of NO_2, SO_2, and CO displayed variation trends similar to that

298   of the particle concentration. The fluctuations of trace gas concentrations were caused by primary

299   emission and secondary processes. Noticeably, the concentration of NO increased dramatically in rush

300   hours during the haze period, whereas it fluctuated slightly during the clean period; indicating that local

301   emissions were easily accumulated under stagnant atmosphere. In addition, the maximum concentration

302   of O_3 remained considerably higher during daytime, whereas it decreased significantly at night. The most

303   plausible explanation is that O_3 was consumed rapidly by the accumulated trace gases, such as NO_x, and

304   VOCs.

305   **3.5 Variations of hygroscopicity and effective density during the PM episode**

306   Figure 6 shows the averaged hygroscopicity and effective density for different pollution periods of the

307   PM episode. Regardless of the pollution period, the nearly-hydrophobic particles were externally mixed

308   with some hygroscopic particles. During the clean period, the more-hygroscopic particles dominated the

309   40 nm particle population, indicating that the near-hydrophobic primary particles were rapidly dispersed

310   due to atmospheric dilution. The number fraction of the near-hydrophobic group for different sizes

311   increased as the PM episode developed, indicative of the increasing accumulation of local emissions.

312   Notably, the increase of the near-hydrophobic particles with the evolution of the PM episode become less

313   significant as particle size increased, indicating that primary emission exerted a more significant impact

314   on smaller particles than on larger ones. The median diameter of nascent traffic particles from various

315   gasoline sources ranged between 55 and 73 nm with an average of 65 nm (Momenimovahed and Olfert,

316   2015). Therefore, the number fraction of the near-hydrophobic particles larger than 200 nm is not sensitive

317   to the accumulation of traffic emissions.

318   Interestingly, the variations of particle effective density for different sizes are in good agreement with

319   the hygroscopicity. The dominant peak of effective density distribution appeared at $\rho_{eff} = \sim 1.5$ g cm^{-3} for

320   40 nm particles in the clean period, indicating that they are highly aged with hygroscopic inorganic salts

321   (Yin et al., 2015). As the episode developed, the mean density shifted to lower values, indicating the

322   increasing contribution of lower density carbonaceous materials. The averaged density distribution was

323   broadened as the episode developed, suggesting that it could be deconvolved into two groups and that the

324 number fraction of the low-density group increased. This finding revealed that the lower density particles

325 are less hygroscopic whereas the larger density group corresponds to the more-hygroscopic one. In

326 addition, the variations of hygroscopicity and effective density coincided with the evolution of PBL height,

327 indicating that the increasing accumulation of local emissions due to adverse atmospheric conditions is

328 likely responsible for the enhancement of those near-hydrophobic and lower density particles.

329   Figure 7 displays the temporal profiles for contributions of EC (including bare EC and OC-coated EC),

330 OC, sulfate, and nitrate determined by SPAMS. Obviously, the relative contribution of nitrate increased

331 as the episode developed. In contrast, the relative contribution of sulfate displayed an opposite trend. This

332 feature is comparable with the aforementioned results of SNA, thus further highlighting the important

333 role of nitrate in haze formation in Shanghai. The number fraction of EC particles generally increased

334 during the haze period, peaking at midnight on 9 and 10 January. It should be pointed out that the

335 measured number fraction possibly underestimated the contribution of EC particles because the dominant

336 size range of fresh traffic particles is below the detection limit of SPAMS (0.2–2.0 μm). This finding

337 provides good support for the increase of near-hydrophobic and lower density particles as the episode

338 developed. Niu et al. (2016) reported that the number ratio of secondary particles to soot in haze samples

339 was higher than that collected in the clean days in Beijing. Our finding is comparable to their results. In

340 contrast, the number fraction of pure OC decreased during the pollution event. The possible explanation

341 is that the condensation of organic matter was favored on the large amount of preexisting EC particles, or

342   that photo-oxidation of VOCs was minimized due to lower solar radiation.

3.6 Evolutions of hygroscopicity and effective density with particle growth

344   As shown in Fig. 5, three "banana-shaped" evolutions of the particle size distribution were identified

345   in the representative PM episode. The banana-type contour plot of particle size distributions is a typical

346   characteristics of new particle formation (NPF) events and traditionally regarded as one of the most

347   important criteria for identifying NPF (Xiao et al., 2015;Dal Maso et al., 2005;Levy et al., 2013;Zhang et

348   al., 2012). Atmospheric NPF is often defined by the burst of nucleation mode particles and subsequent

349   growth of the nuclei to larger particles (Zhang et al., 2012;Kulmala et al., 2012). Gas-phase sulfuric acid

350   produced via oxidation of SO_2 by OH radical plays a dominant role in the NPF events. NPF is typically

351   completely suppressed when preexisting particles is abundant, because gas-phase sulfuric acid is rapidly

352   lost to the surfaces of preexisting aerosols (Zhang et al., 2012). In addition to sulfuric acid, low-volatility

353   organic species, and interaction between sulfate and organics are important for NPF (Zhang et al.,

354   2004;Zhao et al., 2009). However, the possibility of NPF can be ignored in this study due to the absence

355   of the burst of nucleation mode particles and the high concentration of $PM_{1.0}$. The burst of Aitken mode

356   particles in the current study may be attributable to rapid accumulation of traffic emissions during rush

357   hours under stagnant atmospheric conditions. The "banana-shaped" particle growth in the time evolution

358   of particle size distribution from the Aitken mode size range to accumulation mode size range was

359   primarily due to coagulation and condensation processes. This feature provided an excellent opportunity

360   to reveal the chemical mechanism of particle growth during the PM episode.

361   The first "banana-shaped" evolution of the particle size distribution occurred from approximately

362   05:00 to 15:00 LT on 9 January, with increase of the particle number concentration (N_{total}) from 1.7×10^4

363   to 3.4×10^4 cm^{-3} followed by a decrease trend until 17:00 LT (Period 1). The second "banana-shaped"

364   evolution occurred from approximately 18:00 LT on 9 January to approximately 12:00 LT on 10 January

365   (Period 2). The N_{total} increased from 2.1×10^4 to 4.2×10^4 cm^{-3} within 3 h, followed by gradual decrease of

366   N_{total} in contrast to a continuous increase of the particle mass concentration. During the growth process,

367   the mode diameter of the particle population increased from below 40 nm to approximately 200 nm. The

368   third "banana-shaped" evolution began in the evening rush hours on 10 January, with the continuous

369   increase of PM mass concentration for 12 h (Period 3). The latter two banana-shaped evolutions lasted

370   long enough to tracer the changes in hygroscopicity and effective density due to particle growth.

371   Figure 8 illustrates the evolution of particle hygroscopicity and effective density during periods 2 and

372   3. During the initial stage, the measured GF and effective density distributions were both bimodal, with

373   a dominant peak at GF = ~1.0 and ρ_{eff} = ~1.0 g cm^{-3}, respectively. In a previous study, we found that the

374   number fraction of near-hydrophobic particles varied with the traffic exhaust (Ye et al., 2013). Moreover,

375   laboratory studies showed that the effective density of 50 nm vehicle particles was approximately 1.0 g

376   cm^{-3} (Olfert et al., 2007;Park et al., 2003;Momenimovahed and Olfert, 2015). These findings indicate that

377   the initial burst of Aitken mode particles is attributable to the presence of enhanced traffic-related

378   emissions. In contrast, the number fraction and GF of the more-hygroscopic group increased with the

379   growing particle size, indicating the addition of hygroscopic inorganic species. The variation of the

380   effective density of the particles was similar to that of the hygroscopicity, indicating the increase of high

381   density materials. In general, inorganic sulfate and nitrate are more hygroscopic and denser than soot

382   particles or organic aerosols (Yin et al., 2015). These findings suggest that secondary sulfate and nitrate

383   increased with the growing particle size, indicating the importance of the conversion of SO_2 and NO_x in

384   particle growth. This conclusion is supported by the largest SNA concentration in $PM_{1.0}$ during the PM

385   episode (31.3 μg m^{-3} on 10 January and 23.8 μg m^{-3} on 11 January). Considering that the concentration

386   of nitrate was much higher than that of sulfate during the haze event, the increase of hygroscopicity was

387   dominated by the addition of nitrate.

388

389   **4. Conclusions**

390   Particle size distribution, size-resolved hygroscopic growth and effective density of sub-micrometer

391   aerosols were determined using a HTDMA-APM system, along with measurements of cascade impactor

392   samples and single particle mass spectrometry in urban Shanghai during winter 2014.

393   The PM episode exhibited a periodic cycle of ~5 days. The average concentration of $PM_{2.5}$ was 87 $\pm$

394   67 μg m^{-3}, with approximately 62% of hourly $PM_{2.5}$ concentrations exceeding the Chinese Grade II

395   guideline. Both secondary inorganic salts and carbonaceous aerosols contributed substantially to haze

396   formation, because the mass ratio of SNA/$PM_{1.0}$ fluctuated slightly around 0.28 during the observation

397   period. Nitrate became the most abundant ionic species at $PM_{1.0}$ >40 μg m^{-3}, indicating that the sources

398   of nitrate contributed more to haze formation in Shanghai than did SO_2.

399   The severe haze pollution was likely triggered by the adverse meteorological conditions, which favored

400   the accumulation of local emissions and subsequent rapid growth to larger particles. As the PM episode

401   developed, the number fraction of nearly-hydrophobic particles of different size increased, consistent with

402   decrease of the mean effective density. Both hygroscopicity and effective density of the particles were

403   found to increase considerably with growing particle size, indicating that secondary aerosol formation

404   was one of the most important contributors to particle growth. Our results suggest that the accumulation

405   of local emissions under adverse meteorological conditions and subsequent rapid particle growth by

406   secondary processes are primarily responsible for the haze pollution in Shanghai during wintertime.

407

408   *Acknowledgments.* This work was supported by the National Natural Science Foundation of China

409   (21477020, 21527814, and 91544224), and the National Science and Technology Support Program of

410   China (2014BAC22B01).

411

412   Reference

413   Aggarwal, S. G., Mochida, M., Kitamori, Y., and Kawamura, K.: Chemical closure study on hygroscopic

properties of urban aerosol particles in Sapporo, Japan, Environmental Science & Technology, 41, 6920-6925, 10.1021/es063092m, 2007.

Chen, D., Liu, Z., Fast, J., and Ban, J.: Simulations of sulfate-nitrate-ammonium (SNA) aerosols during the extreme haze events over northern China in October 2014, Atmospheric Chemistry and Physics, 16, 10707-10724, 10.5194/acp-16-10707-2016, 2016.

Chu, B., Zhang, X., Liu, Y., He, H., Sun, Y., Jiang, J., Li, J., and Hao, J.: Synergetic formation of secondary inorganic and organic aerosol: effect of SO2 and NH3 on particle formation and growth, Atmospheric Chemistry and Physics, 16, 14219-14230, 10.5194/acp-16-14219-2016, 2016.

Dal Maso, M., Kulmala, M., Riipinen, I., Wagner, R., Hussein, T., Aalto, P. P., and Lehtinen, K. E. J.: Formation and growth of fresh atmospheric aerosols: eight years of aerosol size distribution data from SMEAR II, Hyytiala, Finland, Boreal Environment Research, 10, 323-336, 2005.

Dinar, E., Mentel, T. F., and Rudich, Y.: The density of humic acids and humic like substances (HULIS) from fresh and aged wood burning and pollution aerosol particles, Atmospheric Chemistry and Physics, 6, 5213-5224, 2006.

Fu, Q. Y., Zhuang, G. S., Wang, J., Xu, C., Huang, K., Li, J., Hou, B., Lu, T., and Streets, D. G.: Mechanism of formation of the heaviest pollution episode ever recorded in the Yangtze River Delta, China, Atmospheric Environment, 42, 2023-2036, 2008.

Gasparini, R., Li, R. J., Collins, D. R., Ferrare, R. A., and Brackett, V. G.: Application of aerosol hygroscopicity measured at the Atmospheric Radiation Measurement Program's Southern Great Plains site to examine composition and evolution, J. Geophys. Res.-Atmos., 111, D05S12, doi:10.1029/2004JD005448, 10.1029/2004jd005448, 2006.

Guan, W. J., Zheng, X. Y., Chung, K. F., and Zhong, N. S.: Impact of air pollution on the burden of chronic respiratory diseases in China: time for urgent action, Lancet, 388, 1939-1951, 2016.

Guo, S., Hu, M., Guo, Q., Zhang, X., Schauer, J. J., and Zhang, R.: Quantitative evaluation of emission controls on primary and secondary organic aerosol sources during Beijing 2008 Olympics, Atmospheric Chemistry and Physics, 13, 8303-8314, 10.5194/acp-13-8303-2013, 2013.

Guo, S., Hu, M., Zamora, M. L., Peng, J., Shang, D., Zheng, J., Du, Z., Wu, Z., Shao, M., Zeng, L., Molina, M. J., and Zhang, R.: Elucidating severe urban haze formation in China, Proceedings of the National Academy of Sciences of the United States of America, 111, 17373-17378, 10.1073/pnas.1419604111, 2014.

Gysel, M., Crosier, J., Topping, D. O., Whitehead, J. D., Bower, K. N., Cubison, M. J., Williams, P. I., Flynn, M. J., McFiggans, G. B., and Coe, H.: Closure study between chemical composition and hygroscopic growth of aerosol particles during TORCH2, Atmospheric Chemistry and Physics, 7, 6131-6144, 2007.

Gysel, M., McFiggans, G. B., and Coe, H.: Inversion of tandem differential mobility analyser (TDMA)

measurements, Journal of Aerosol Science, 40, 134-151, 10.1016/j.jaerosci.2008.07.013, 2009.

Han, B., Zhang, R., Yang, W., Bai, Z., Ma, Z., and Zhang, W.: Heavy haze episodes in Beijing during January 2013: Inorganic ion chemistry and source analysis using highly time-resolved measurements from an urban site, Science of The Total Environment, 544, 319-329, http://dx.doi.org/10.1016/j.scitotenv.2015.10.053, 2016.

Heal, M. R., Kumar, P., and Harrison, R. M.: Particles, air quality, policy and health, Chemical Society Reviews, 41, 6606-6630, 10.1039/c2cs35076a, 2012.

Hu, M., Peng, J., Sun, K., Yue, D., Guo, S., Wiedensohler, A., and Wu, Z.: Estimation of size-resolved ambient particle density based on the measurement of aerosol number, mass, and chemical size distributions in the winter in Beijing, Environ Sci Technol, 46, 9941-9947, 10.1021/es204073t, 2012.

Hu, Q. Q., Fu, H. B., Wang, Z. Z., Kong, L. D., Chen, M. D., and Chen, J. M.: The variation of characteristics of individual particles during the haze evolution in the urban Shanghai atmosphere, Atmospheric Research, 181, 95-105, 10.1016/j.atmosres.2016.06.016, 2016.

Huang, R.-J., Zhang, Y., Bozzetti, C., Ho, K.-F., Cao, J.-J., Han, Y., Daellenbach, K. R., Slowik, J. G., Platt, S. M., Canonaco, F., Zotter, P., Wolf, R., Pieber, S. M., Bruns, E. A., Crippa, M., Ciarelli, G., Piazzalunga, A., Schwikowski, M., Abbaszade, G., Schnelle-Kreis, J., Zimmermann, R., An, Z., Szidat, S., Baltensperger, U., El Haddad, I., and Prevot, A. S. H.: High secondary aerosol contribution to particulate pollution during haze events in China, Nature, 514, 218-222, 10.1038/nature13774, 2014.

IPCC: Climate Change 2013: The Physical Science Basis, Cambridge, UK, 2013.

Khalizov, A. F., Xue, H., Wang, L., Zheng, J., and Zhang, R.: Enhanced Light Absorption and Scattering by Carbon Soot Aerosol Internally Mixed with Sulfuric Acid, Journal of Physical Chemistry A, 113, 1066-1074, 10.1021/jp807531n, 2009.

Kulmala, M., Petaja, T., Nieminen, T., Sipila, M., Manninen, H. E., Lehtipalo, K., Dal Maso, M., Aalto, P. P., Junninen, H., Paasonen, P., Riipinen, I., Lehtinen, K. E., Laaksonen, A., and Kerminen, V. M.: Measurement of the nucleation of atmospheric aerosol particles, Nature protocols, 7, 1651-1667, 10.1038/nprot.2012.091, 2012.

Levy, M. E., Zhang, R. Y., Khalizov, A. F., Zheng, J., Collins, D. R., Glen, C. R., Wang, Y., Yu, X. Y., Luke, W., Jayne, J. T., and Olaguer, E.: Measurements of submicron aerosols in Houston, Texas during the 2009 SHARP field campaign, J. Geophys. Res.-Atmos., 118, 10518-10534, 10.1002/jgrd.50785, 2013.

Levy, M. E., Zhang, R. Y., Zheng, J., Tan, H. B., Wang, Y., Molina, L. T., Takahama, S., Russell, L. M., and Li, G. H.: Measurements of submicron aerosols at the California-Mexico border during the Cal-Mex 2010 field campaign, Atmospheric Environment, 88, 308-319, 10.1016/j.atmosenv.2013.08.062, 2014.

Li, J. J., Wang, G. H., Ren, Y. Q., Wang, J. Y., Wu, C., Han, Y. N., Zhang, L., Cheng, C. L., and Meng, J. J.: Identification of chemical compositions and sources of atmospheric aerosols in Xi'an, inland China during two types of haze events, Science of the Total Environment, 566, 230-237,

484   10.1016/j.scitotenv.2016.05.057, 2016.

485   Li, L., Huang, Z. X., Dong, J. G., Li, M., Gao, W., Nian, H. Q., Fu, Z., Zhang, G. H., Bi, X. H., Cheng,
486   P., and Zhou, Z.: Real time bipolar time-of-flight mass spectrometer for analyzing single aerosol particles,
487   International Journal of Mass Spectrometry, 303, 118-124, 10.1016/j.ijms.2011.01.017, 2011.

488   Li, P., Yan, R., Yu, S., Wang, S., Liu, W., and Bao, H.: Reinstate regional transport of $PM_{2.5}$ as a major
489   cause of severe haze in Beijing, Proceedings of the National Academy of Sciences of the United States of
490   America, 112, E2739-E2740, 10.1073/pnas.1502596112, 2015.

491   Lin, Y., Huang, K., Zhuang, G., Fu, J. S., Wang, Q., Liu, T., Deng, C., and Fu, Q.: A multi-year evolution
492   of aerosol chemistry impacting visibility and haze formation over an Eastern Asia megacity, Shanghai,
493   Atmospheric Environment, 92, 76-86, 10.1016/j.atmosenv.2014.04.007, 2014.

494   Liu, H. J., Zhao, C. S., Nekat, B., Ma, N., Wiedensohler, A., van Pinxteren, D., Spindler, G., Müller, K.,
495   and Herrmann, H.: Aerosol hygroscopicity derived from size-segregated chemical composition and its
496   parameterization in the North China Plain, Atmospheric Chemistry and Physics, 14, 2525-2539,
497   10.5194/acp-14-2525-2014, 2014.

498   Malloy, Q. G. J., Nakao, S., Qi, L., Austin, R., Stothers, C., Hagino, H., and Cocker, D. R.: Real-Time
499   Aerosol Density Determination Utilizing a Modified Scanning Mobility Particle SizerAerosol Particle
500   Mass Analyzer System, Aerosol Science and Technology, 43, 673-678, 10.1080/02786820902832960,
501   2009.

502   Massling, A., Stock, M., Wehner, B., Wu, Z. J., Hu, M., Bruggemann, E., Gnauk, T., Herrmann, H., and
503   Wiedensohler, A.: Size segregated water uptake of the urban submicrometer aerosol in Beijing,
504   Atmospheric Environment, 43, 1578-1589, 2009.

505   Momenimovahed, A., and Olfert, J. S.: Effective density and volatility of particles emitted from gasoline
506   direct injection vehicles and implications for particle mass measurement, Aerosol Sci. Technol., 49, 1051-
507   1062, 10.1080/02786826.2015.1094181, 2015.

508   Niu, H. Y., Hu, W., Zhang, D. Z., Wu, Z. J., Guo, S., Pian, W., Cheng, W. J., and Hu, M.: Variations of
509   fine particle physiochemical properties during a heavy haze episode in the winter of Beijing, Science of
510   the Total Environment, 571, 103-109, 10.1016/j.scitotenv.2016.07.147, 2016.

511   Olfert, J. S., Symonds, J. P. R., and Collings, N.: The effective density and fractal dimension of particles
512   emitted from a light-duty diesel vehicle with a diesel oxidation catalyst, Journal of Aerosol Science, 38,
513   69-82, 10.1016/j.jaerosci.2006.10.002, 2007.

514   Pagels, J., Khalizov, A. F., McMurry, P. H., and Zhang, R. Y.: Processing of Soot by Controlled Sulphuric
515   Acid and Water CondensationMass and Mobility Relationship, Aerosol Sci. Technol., 43, 629-640,
516   10.1080/02786820902810685, 2009.

517   Park, K., F., C., Kittelson, D. B., and McMurry, P. H.: Relationship between particle mass and mobility
518   for diesel exhaust particles Environmental Science and Technology, 37, 577-583, 2003.

Peng, J., Hu, M., Guo, S., Du, Z., Zheng, J., Shang, D., Zamora, M. L., Zeng, L., Shao, M., Wu, Y.-S., Zheng, J., Wang, Y., Glen, C. R., Collins, D. R., Molina, M. J., and Zhang, R.: Markedly enhanced absorption and direct radiative forcing of black carbon under polluted urban environments, Proceedings of the National Academy of Sciences of the United States of America, 113, 4266-4271, 10.1073/pnas.1602310113, 2016.

Petters, M. D., and Kreidenweis, S. M.: A single parameter representation of hygroscopic growth and cloud condensation nucleus activity, Atmospheric Chemistry and Physics, 7, 1961-1971, 2007.

Qiao, T., Zhao, M., Xiu, G., and Yu, J.: Simultaneous monitoring and compositions analysis of PM_1 and $PM_{2.5}$ in Shanghai: Implications for characterization of haze pollution and source apportionment, The Science of the total environment, 557-558, 386-394, 10.1016/j.scitotenv.2016.03.095, 2016.

Rissler, J., Nordin, E. Z., Eriksson, A. C., Nilsson, P. T., Frosch, M., Sporre, M. K., Wierzbicka, A., Svenningsson, B., Londahl, J., Messing, M. E., Sjogren, S., Hemmingsen, J. G., Loft, S., Pagels, J. H., and Swietlicki, E.: Effective density and mixing state of aerosol particles in a near-traffic urban environment, Environ Sci Technol, 48, 6300-6308, 10.1021/es5000353, 2014.

Shi, Y., Chen, J., Hu, D., Wang, L., Yang, X., and Wang, X.: Airborne submicron particulate (PM_1) pollution in Shanghai, China: Chemical variability, formation/dissociation of associated semi-volatile components and the impacts on visibility, Science of the Total Environment, 473, 199-206, 10.1016/j.scitotenv.2013.12.024, 2014.

Spencer, M. T., Shields, L. G., and Prather, K. A.: Simultaneous measurement of the effective density and chemical composition of ambient aerosol particles, Environmental Science & Technology, 41, 1303-1309, 10.1021/es061425+, 2007.

Sun, Y. L., Chen, C., Zhang, Y. J., Xu, W. Q., Zhou, L. B., Cheng, X. L., Zheng, H. T., Ji, D. S., Li, J., Tang, X., Fu, P. Q., and Wang, Z. F.: Rapid formation and evolution of an extreme haze episode in Northern China during winter 2015, Scientific Reports, 6, 10.1038/srep27151, 2016.

Swietlicki, E., Hansson, H. C., Hameri, K., Svenningsson, B., Massling, A., McFiggans, G., McMurry, P. H., Petaja, T., Tunved, P., Gysel, M., Topping, D., Weingartner, E., Baltensperger, U., Rissler, J., Wiedensohler, A., and Kulmala, M.: Hygroscopic properties of submicrometer atmospheric aerosol particles measured with H-TDMA instruments in various environments - a review, Tellus Ser. B-Chem. Phys. Meteorol., 60, 432-469, 10.1111/j.1600-0889.2008.00350.x, 2008.

Tao, Y., Ye, X. N., Ma, Z., Xie, Y. Y., Wang, R. Y., Chen, J. M., Yang, X., and Jiang, S. Q.: Insights into different nitrate formation mechanisms from seasonal variations of secondary inorganic aerosols in Shanghai, Atmospheric Environment, 145, 1-9, 10.1016/j.atmosenv.2016.09.012, 2016.

Topping, D. O., McFiggans, G. B., and Coe, H.: A curved multi-component aerosol hygroscopicity model framework: Part 1 - Inorganic compounds, Atmospheric Chemistry and Physics, 5, 1205-1222, 2005.

Turpin, B. J., and Lim, H. J.: Species contributions to PM2.5 mass concentrations: Revisiting common

assumptions for estimating organic mass, Aerosol Science and Technology, 35, 602-610, 10.1080/02786820152051454, 2001.

Wang, G., Zhang, R., Gomez, M. E., Yang, L., Zamora, M. L., Hu, M., Lin, Y., Peng, J., Guo, S., Meng, J., Li, J., Cheng, C., Hu, T., Ren, Y., Wang, Y., Gao, J., Cao, J., An, Z., Zhou, W., Li, G., Wang, J., Tian, P., Marrero-Ortiz, W., Secrest, J., Du, Z., Zheng, J., Shang, D., Zeng, L., Shao, M., Wang, W., Huang, Y., Wang, Y., Zhu, Y., Li, Y., Hu, J., Pan, B., Cai, L., Cheng, Y., Ji, Y., Zhang, F., Rosenfeld, D., Liss, P. S., Duce, R. A., Kolb, C. E., and Molina, M. J.: Persistent sulfate formation from London Fog to Chinese haze, Proceedings of the National Academy of Sciences of the United States of America, 113, 13630-13635, 10.1073/pnas.1616540113, 2016.

Wang, H., Xu, J., Zhang, M., Yang, Y., Shen, X., Wang, Y., Chen, D., and Guo, J.: A study of the meteorological causes of a prolonged and severe haze episode in January 2013 over central-eastern China, Atmospheric Environment, 98, 146-157, 10.1016/j.atmosenv.2014.08.053, 2014a.

Wang, Y., Wan, Q., Meng, W., Liao, F., Tan, H., and Zhang, R.: Long-term impacts of aerosols on precipitation and lightning over the Pearl River Delta megacity area in China, Atmospheric Chemistry and Physics, 11, 12421-12436, 10.5194/acp-11-12421-2011, 2011.

Wang, Y., Khalizov, A., Levy, M., and Zhang, R.: New Directions: Light absorbing aerosols and their atmospheric impacts, Atmospheric Environment, 81, 713-715, 10.1016/j.atmosenv.2013.09.034, 2013.

Wang, Y., Zhang, Q., Jiang, J., Zhou, W., Wang, B., He, K., Duan, F., Zhang, Q., Philip, S., and Xie, Y.: Enhanced sulfate formation during China's severe winter haze episode in January 2013 missing from current models, J. Geophys. Res.-Atmos., 119, 10.1002/2013jd021426, 2014b.

Wang, Y., Zhang, R., and Saravanan, R.: Asian pollution climatically modulates mid-latitude cyclones following hierarchical modelling and observational analysis, Nature Communications, 5, 10.1038/ncomms4098, 2014c.

Wang, Y. H., Liu, Z. R., Zhang, J. K., Hu, B., Ji, D. S., Yu, Y. C., and Wang, Y. S.: Aerosol physicochemical properties and implications for visibility during an intense haze episode during winter in Beijing, Atmospheric Chemistry and Physics, 15, 3205-3215, 10.5194/acp-15-3205-2015, 2015.

Wu, G., Li, Z., Fu, C., Zhang, X., Zhang, R., Zhang, R., Zhou, T., Li, J., Li, J., Zhou, D., Wu, L., Zhou, L., He, B., and Huang, R.: Advances in studying interactions between aerosols and monsoon in China, Science China-Earth Sciences, 59, 1-16, 10.1007/s11430-015-5198-z, 2016a.

Wu, S., Ni, Y., Li, H., Pan, L., Yang, D., Baccarelli, A. A., Deng, F., Chen, Y., Shima, M., and Guo, X.: Short-term exposure to high ambient air pollution increases airway inflammation and respiratory symptoms in chronic obstructive pulmonary disease patients in Beijing, China, Environment International, 94, 76-82, 10.1016/j.envint.2016.05.004, 2016b.

Wu, Z. J., Zheng, J., Shang, D. J., Du, Z. F., Wu, Y. S., Zeng, L. M., Wiedensohler, A., and Hu, M.: Particle hygroscopicity and its link to chemical composition in the urban atmosphere of Beijing, China, during

589 summertime, Atmospheric Chemistry and Physics, 16, 1123-1138, 10.5194/acp-16-1123-2016, 2016c.

590 Xiao, S., Wang, Q. Y., Cao, J. J., Huang, R. J., Chen, W. D., Han, Y. M., Xu, H. M., Liu, S. X., Zhou, Y.
591 Q., Wang, P., Zhang, J. Q., and Zhan, C. L.: Long-term trends in visibility and impacts of aerosol
592 composition on visibility impairment in Baoji, China, Atmospheric Research, 149, 88-95,
593 10.1016/j.atmosres.2014.06.006, 2014.

594 Xiao, S., Wang, M. Y., Yao, L., Kulmala, M., Zhou, B., Yang, X., Chen, J. M., Wang, D. F., Fu, Q. Y.,
595 Worsnop, D. R., and Wang, L.: Strong atmospheric new particle formation in winter in urban Shanghai,
596 China, Atmospheric Chemistry and Physics, 15, 1769-1781, 10.5194/acp-15-1769-2015, 2015.

597 Xie, Y., Ding, A., Nie, W., Mao, H., Qi, X., Huang, X., Xu, Z., Kerminen, V.-M., Petaja, T., Chi, X.,
598 Virkkula, A., Boy, M., Xue, L., Guo, J., Sun, J., Yang, X., Kulmala, M., and Fu, C.: Enhanced sulfate
599 formation by nitrogen dioxide: Implications from in situ observations at the SORPES station, J. Geophys.
600 Res.-Atmos., 120, 12679-12694, 10.1002/2015jd023607, 2015.

601 Yang, L., Zhou, X., Wang, Z., Zhou, Y., Cheng, S., Xu, P., Gao, X., Nie, W., Wang, X., and Wang, W.:
602 Airborne fine particulate pollution in Jinan, China: Concentrations, chemical compositions and influence
603 on visibility impairment, Atmospheric Environment, 55, 506-514, 10.1016/j.atmosenv.2012.02.029, 2012.

604 Ye, X. N., Chen, T. Y., Hu, D. W., Yang, X., Chen, J. M., Zhang, R. Y., Khakuziv, A. F., and Wang, L.: A
605 multifunctional HTDMA system with a robust temperature control, Advances in Atmospheric Sciences,
606 26, 1235-1240, 10.1007/s00376-009-8134-3, 2009.

607 Ye, X. N., Ma, Z., Hu, D. W., Yang, X., and Chen, J. M.: Size-resolved hygroscopicity of submicrometer
608 urban aerosols in Shanghai during wintertime, Atmospheric Research, 99, 353-364, 2010.

609 Ye, X. N., Ma, Z., Zhang, J. C., Du, H. H., Chen, J. M., Chen, H., Yang, X., Gao, W., and Geng, F. H.:
610 Important role of ammonia on haze formation in Shanghai, Environ Res Lett, 6, Artn 024019
611 Doi 10.1088/1748-9326/6/2/024019, 2011.

612 Ye, X. N., Tang, C., Yin, Z., Chen, J. M., Ma, Z., Kong, L. D., Yang, X., Gao, W., and Geng, F. H.:
613 Hygroscopic growth of urban aerosol particles during the 2009 Mirage-Shanghai Campaign, Atmospheric
614 Environment, 64, 263-269, 10.1016/j.atmosenv.2012.09.064, 2013.

615 Yin, Z., Ye, X., Jiang, S., Tao, Y., Shi, Y., Yang, X., and Chen, J.: Size-resolved effective density of urban
616 aerosols in Shanghai, Atmospheric Environment, 100, 133-140, 10.1016/j.atmosenv.2014.10.055, 2015.

617 Zhang, Q., Quan, J., Tie, X., Li, X., Liu, Q., Gao, Y., and Zhao, D.: Effects of meteorology and secondary
618 particle formation on visibility during heavy haze events in Beijing, China, Science of The Total
619 Environment, 502, 578-584, http://dx.doi.org/10.1016/j.scitotenv.2014.09.079, 2015a.

620 Zhang, R., Khalizov, A., Wang, L., Hu, M., and Xu, W.: Nucleation and Growth of Nanoparticles in the
621 Atmosphere, Chemical Reviews, 112, 1957-2011, 10.1021/cr2001756, 2012.

622 Zhang, R., Guo, S., Zamora, M. L., and Hu, M.: Reply to Li et al.: Insufficient evidence for the
623 contribution of regional transport to severe haze formation in Beijing, Proceedings of the National

624 Academy of Sciences of the United States of America, 112, E2741-E2741, 10.1073/pnas.1503855112,
625 2015b.

626 Zhang, R., Wang, G., Guo, S., Zarnora, M. L., Ying, Q., Lin, Y., Wang, W., Hu, M., and Wang, Y.:
627 Formation of Urban Fine Particulate Matter, Chemical Reviews, 115, 3803-3855,
628 10.1021/acs.chemrev.5b00067, 2015c.

629 Zhang, R. Y., Suh, I., Zhao, J., Zhang, D., Fortner, E. C., Tie, X. X., Molina, L. T., and Molina, M. J.:
630 Atmospheric new particle formation enhanced by organic acids, Science, 304, 1487-1490,
631 10.1126/science.1095139, 2004.

632 Zhang, R. Y., Khalizov, A. F., Pagels, J., Zhang, D., Xue, H. X., and McMurry, P. H.: Variability in
633 morphology, hygroscopicity, and optical properties of soot aerosols during atmospheric processing,
634 Proceedings of the National Academy of Sciences of the United States of America, 105, 10291-10296,
635 2008.

636 Zhao, J., Khalizov, A., Zhang, R., and McGraw, R.: Hydrogen-Bonding Interaction in Molecular
637 Complexes and Clusters of Aerosol Nucleation Precursors, Journal of Physical Chemistry A, 113, 680-
638 689, 10.1021/jp806693r, 2009.

639 Zhao, X. J., Zhao, P. S., Xu, J., Meng, W., Pu, W. W., Dong, F., He, D., and Shi, Q. F.: Analysis of a winter
640 regional haze event and its formation mechanism in the North China Plain, Atmospheric Chemistry and
641 Physics, 13, 5685-5696, 10.5194/acp-13-5685-2013, 2013.

642 Zheng, G. J., Duan, F. K., Su, H., Ma, Y. L., Cheng, Y., Zheng, B., Zhang, Q., Huang, T., Kimoto, T.,
643 Chang, D., Poeschl, U., Cheng, Y. F., and He, K. B.: Exploring the severe winter haze in Beijing: the
644 impact of synoptic weather, regional transport and heterogeneous reactions, Atmospheric Chemistry and
645 Physics, 15, 2969-2983, 10.5194/acp-15-2969-2015, 2015.

646

647 **Figure and Table Captions**

648 Figure 1 Schematic diagram of HTDMA-APM system.

649 Figure 2. Temporal evolutions of $PM_{1.0}$, $PM_{2.5}$, and PM_{10} concentrations during the winter observation.

650 Figure 3 Variations of sulfate, nitrate, and ammonium concentrations as a function of $PM_{1.0}$ mass loading.

651 Figure 4 Box plots showing hygroscopicity parameter and effective density at each dry diameter over the

652 whole observation. The whiskers represent the 5th and 95th percentile, the two borders of box display the

653 25th and 75th percentile, and the band in each box denotes the median.

654 Figure 5 Temporal evolutions of particle number size distribution (A), volume size distribution (B), total

655 number concentration and total volume concentration (C), and $PM_{1.0}$ concentration and calculated PM

656 (less than 600 nm in mobility diameter) concentration during the representative PM episode from 7 to 12

657 January.

658 Figure 6 Evolutions of particle hygroscopic growth factor and effective density for different sizes during

659 the representative PM episode.

660 Figure 7 Temporal evolutions of chemical compositions determined by SPAMS during the representative

661 PM episode.

662 Figure 8 Particle hygroscopicity and density during the two particle growth processes

663

664

665
666
667
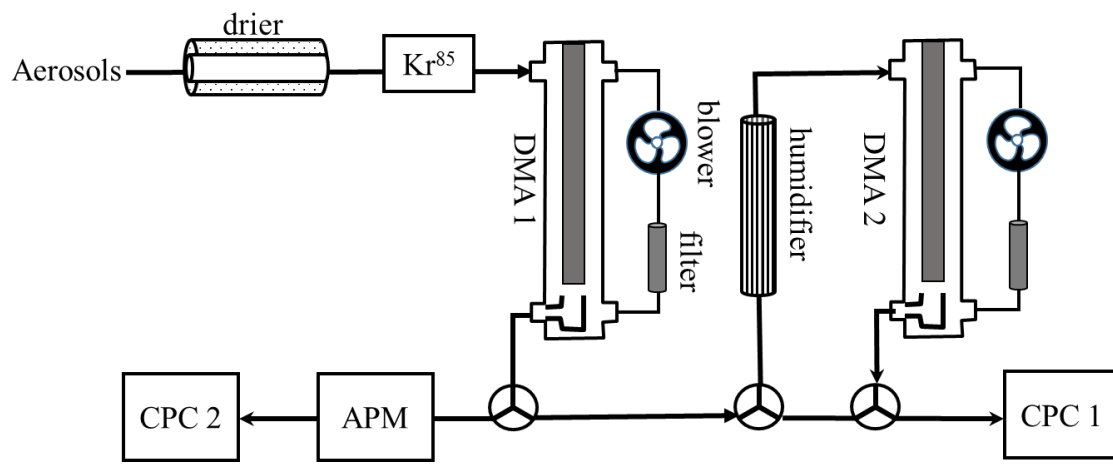
668
669
670
671   Figure 1. Schematic diagram of HTDMA-APM system.

672
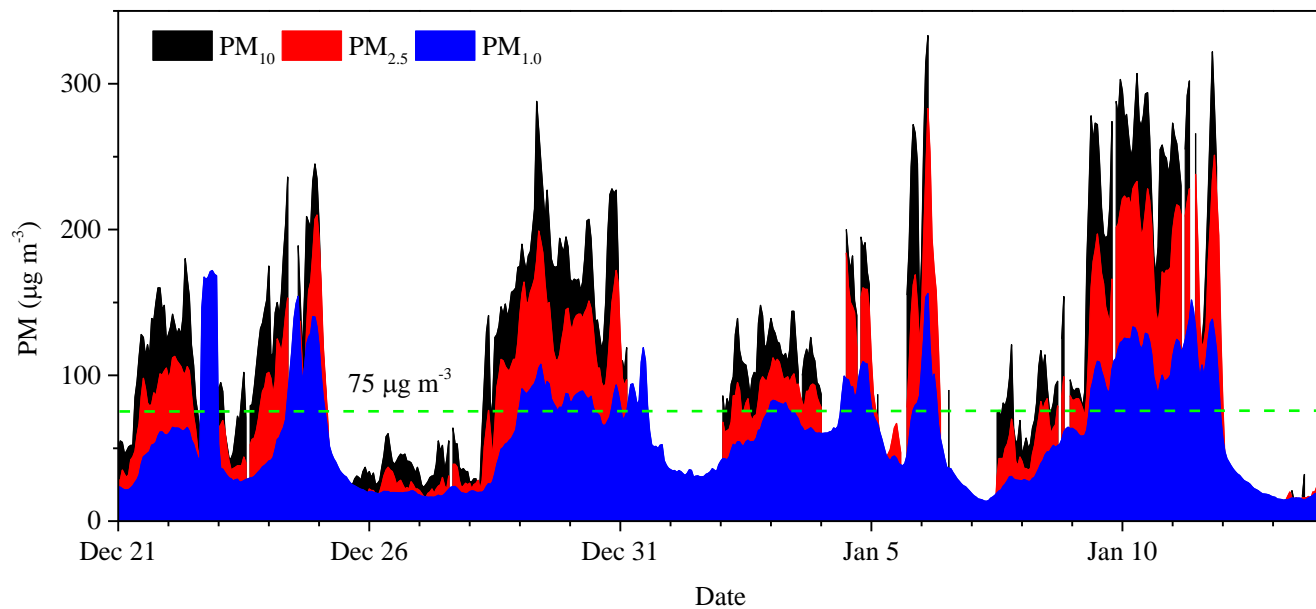
673

674 Figure 2. Temporal evolutions of PM$_{1.0}$, PM$_{2.5}$, and PM$_{10}$ concentrations during the winter observation.

675
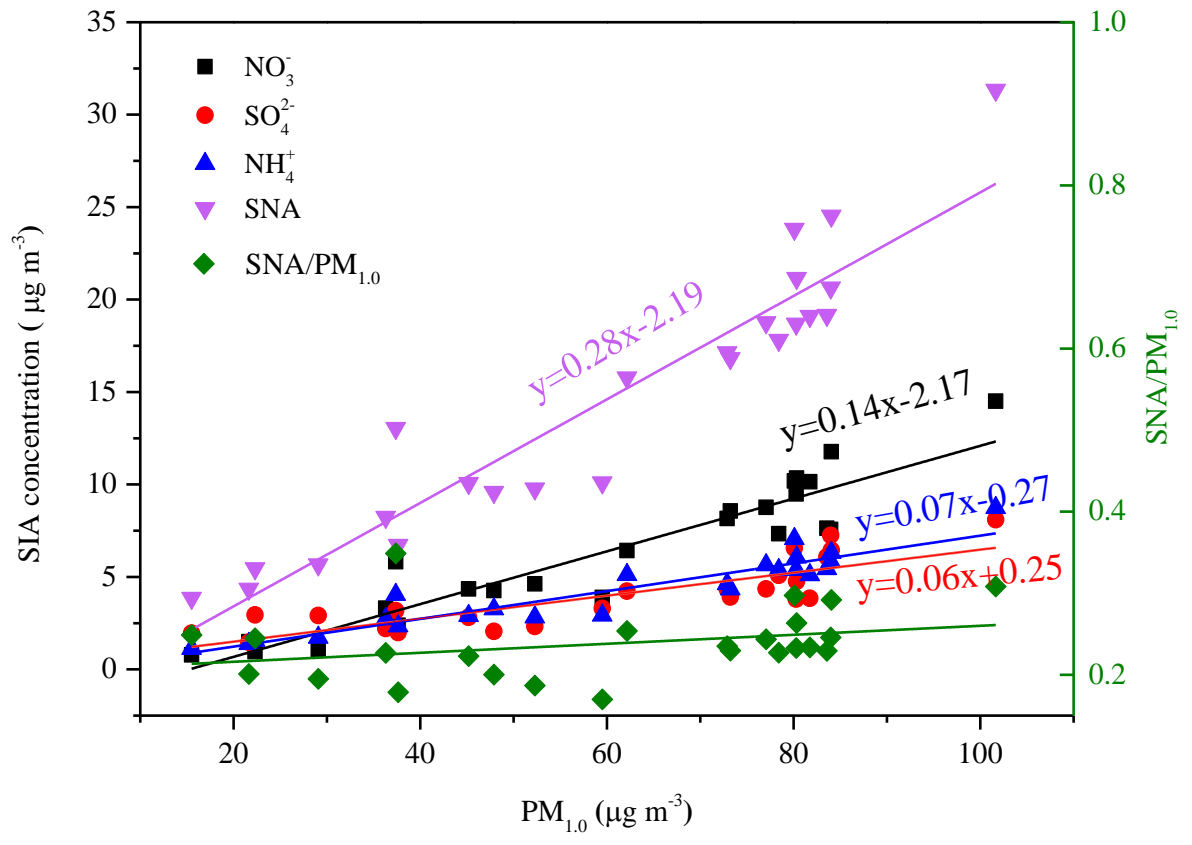
676

677

678 Figure 3. Variations of sulfate, nitrate, and ammonium concentrations as a function of $PM_{1.0}$ mass loading

679
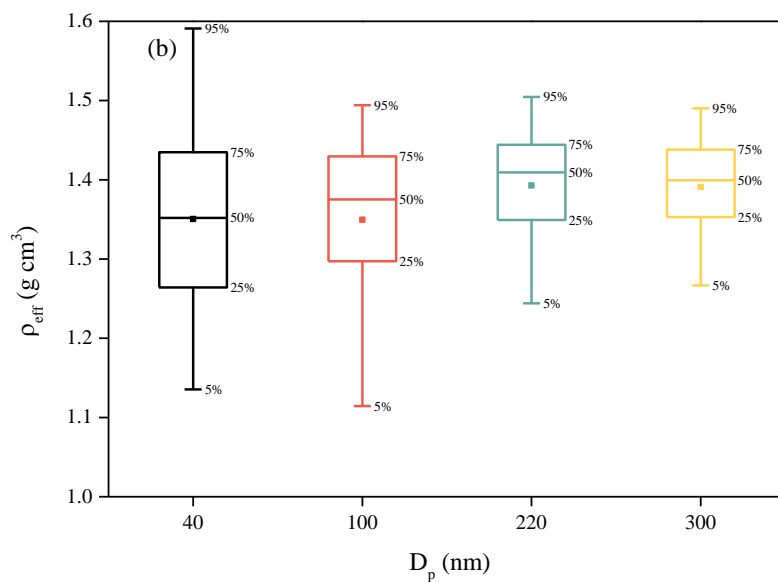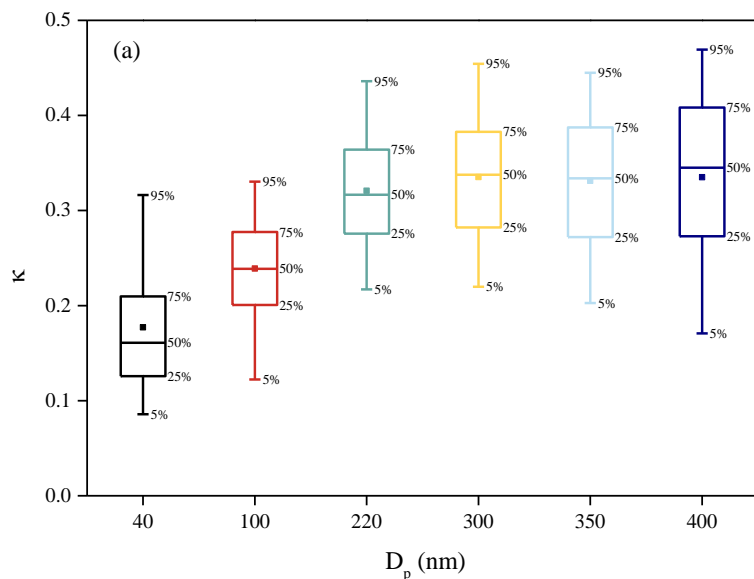
680

681

682   Figure 4. Box plots showing hygroscopicity parameter and effective density at each dry diameter over the

683   whole observation. The whiskers represent the 5th and 95th percentile, the two borders of box display the

684   25th and 75th percentile, and the band in each box denotes the median.
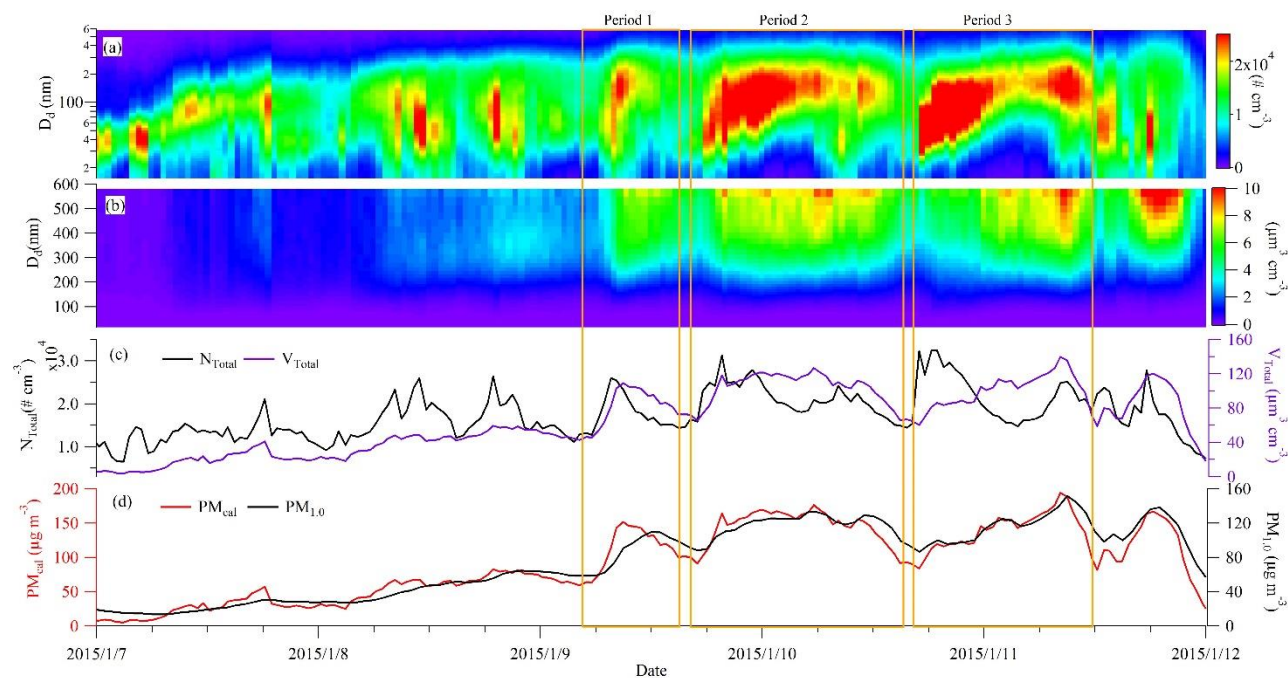
685

686

Figure 5. Temporal evolutions of particle number size distribution (a), volume size distribution (b), total

number concentration and total volume concentration (c), and $PM_{1.0}$ concentration and calculated PM

(less than 600 nm in mobility diameter) concentration (d) during the representative PM episode from 7 to

12 January.

691

692

693
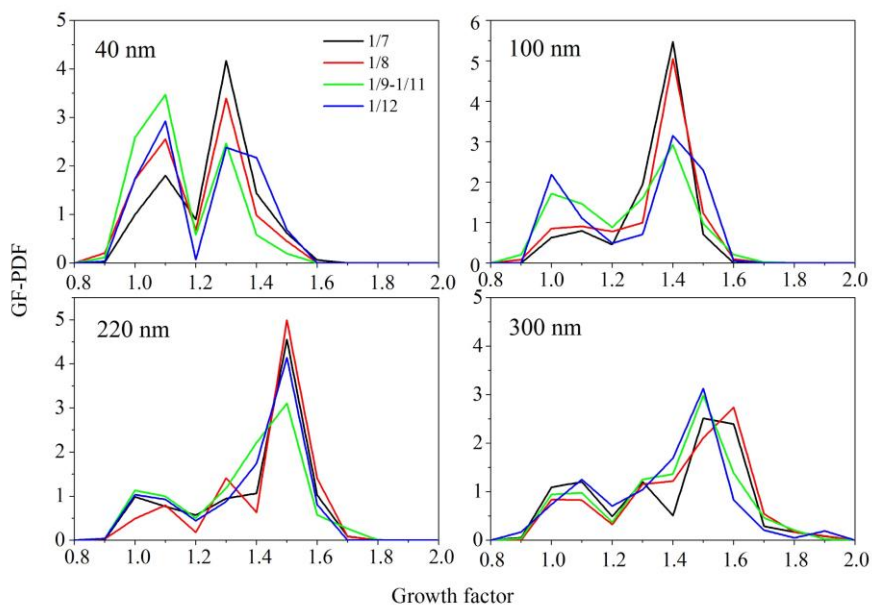
694
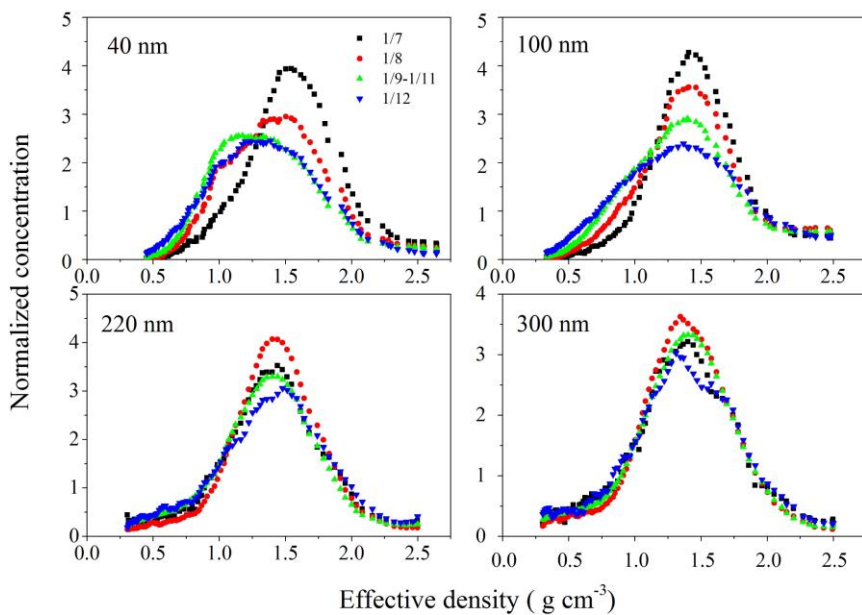
695

696   Figure 6. Evolutions of particle hygroscopic growth factor and effective density for different sizes during

697   the representative PM episode.
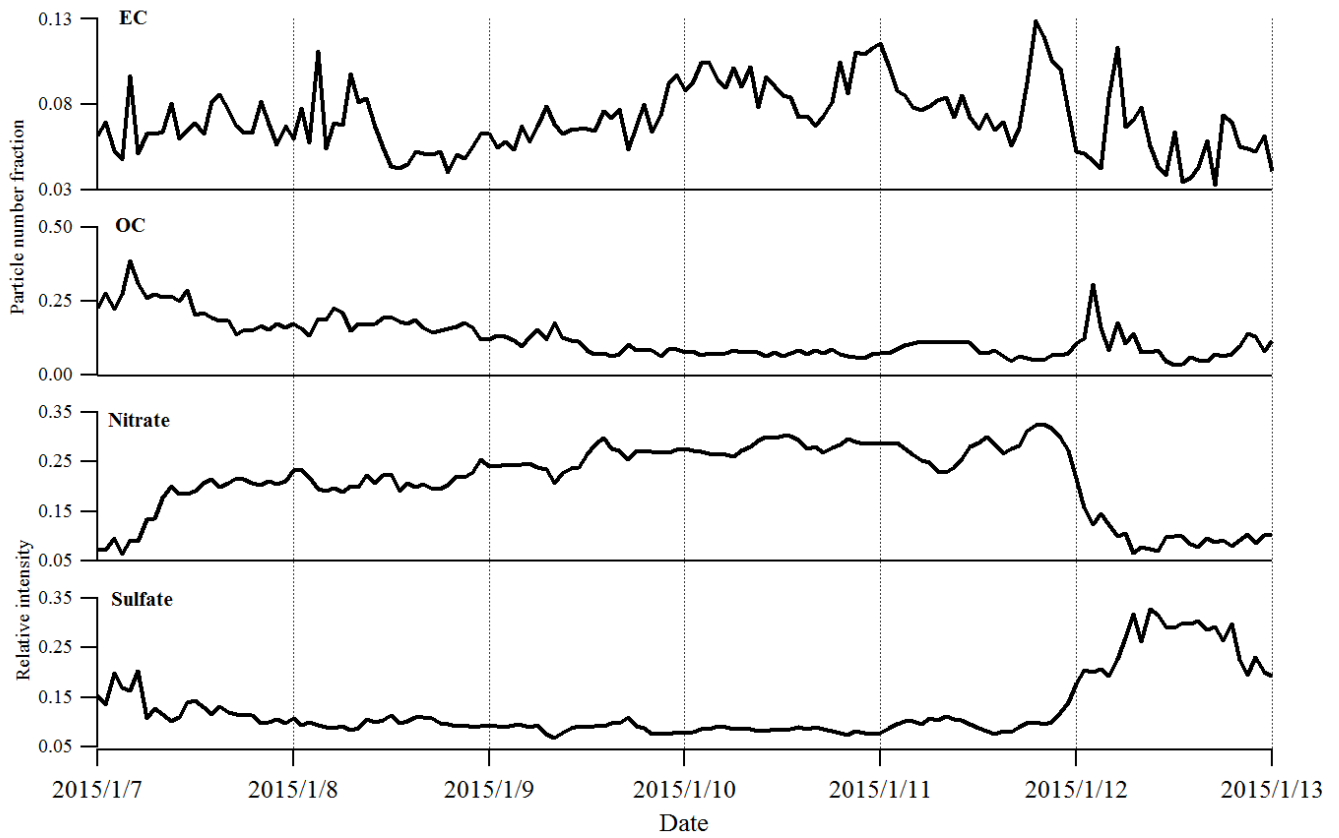
698

699

700 Figure 7. Temporal evolutions of chemical compositions determined by SPAMS during the representative

701 PM episode.

702

703

704

705   Figure 8. Particle hygroscopicity and density during the two particle growth processes.